

The spontaneous elastoresistivity coefficient within the nematic ordered phase of iron pnictides

Joshua J Sanchez¹, Paul Malinowski¹, Joshua Mutch¹, Jian Liu², J-W. Kim³, Philip J Ryan^{3,4}, Jiun-Haw Chu^{1,*}

Affiliation:

¹ Department of Physics, University of Washington, Seattle, Washington 98195, USA.

² Department of Physics and Astronomy, University of Tennessee, Knoxville, Tennessee 37996, USA.

³ Advanced Photon Source, Argonne National Laboratories, Lemont, Illinois 60439, USA.

⁴ School of Physical Sciences, Dublin City University, Dublin 9, Ireland.

*Correspondence to: jhchu@uw.edu (J.-H.C)

Key Words: electronic nematicity, iron-based superconductors, unconventional superconductivity, quantum critical point

Abstract:

When a symmetry is spontaneously broken in solids, a new transport coefficient emerges. A famous example is the anomalous Hall coefficient associated with broken time reversal symmetry. Here we present a measurement of the analogous transport coefficient in solids with broken rotational symmetry, the spontaneous elastoresistivity coefficient, defined as the ratio of the spontaneous resistivity anisotropy to the spontaneous structural distortion. In the iron pnictides, the measured spontaneous elastoresistivity coefficient coincides with the value of the normal elastoresistivity attained at the critical temperature of the nematic phase transition, which in a Landau free energy framework implies that the resistivity anisotropy remains a valid proxy of nematicity above and below the transition. Building on this equality, we find a nearly four-fold enhancement of the spontaneous elastoresistivity coefficient with doping towards optimal superconductivity. Our result reveals a clear sign of quantum critical enhancement of the coupling between nematicity and conduction electrons.

Main Text:

Electronic nematicity refers to a spontaneous rotational symmetry breaking phase in solids driven by electronic correlations¹. Due to the finite electron-lattice coupling, electronic nematicity is always accompanied by a structural phase transition. From a symmetry point of view there is no distinction between a proper ferro-elastic transition and a nematically-driven structural transition. Nevertheless, a method to distinguish these two is the measurement of the elastoresistivity coefficient, which is the ratio of induced resistivity anisotropy to the externally applied anisotropic strain in the same symmetry channel as the nematic ordering². Above the phase transition, the elastoresistivity coefficient $2m_{66}$ is proportional to the B_{2g} nematic susceptibility, the divergence of which is a direct indicator of the electronically-driven instability³⁻⁵. In numerous families of iron-based superconductors, $2m_{66}$ follows a Curie-Weiss temperature dependence over a large temperature and doping range, which established that the structural transition is electronically driven and revealed the prevalence of large nematic fluctuations at temperatures well *above* the phase transition^{2,6,7}.

The proportional relationship between $2m_{66}$ and the B_{2g} nematic susceptibility originates from symmetry considerations. In the tetragonal point group the resistivity anisotropy $\eta = \frac{\rho_{xx} - \rho_{yy}}{\rho_{xx} + \rho_{yy}}$ and the Ising nematic order parameter ψ belong to the same irreducible representation, hence they are linearly proportional to each other in the infinitesimal limit ($\eta = k \psi$)⁸. This symmetry consideration has often been adopted as the argument to treat the resistivity anisotropy as a proxy of the nematic order parameter itself. Nevertheless, resistivity is not a thermodynamic variable and it depends on extrinsic properties such as disorder⁹⁻¹¹. While the perfect Curie-Weiss temperature dependence of $2m_{66}$ implicitly confirms that the proportional constant k is independent of temperature and disorder¹² above the phase transition, it is still unclear whether the constant k is also invariant below the phase transition, especially when the order parameter grows beyond the infinitesimal limit.

Scrutinizing the relationship between resistivity anisotropy and nematicity is also critical to the understanding of superconducting pairing in iron-based materials. Optimal T_c is found in the vicinity of a fully suppressed nematic phase for most families of iron-based high-temperature superconductors. $2m_{66}$ has been shown to diverge towards zero temperature at the optimal doping in several families of materials, suggesting that the superconducting pairing may be enhanced by nematic quantum critical fluctuations¹³. The conduction electrons that participate in pairing are ultimately the same electrons that give rise to the resistivity anisotropy, and so the constant k that quantifies the coupling of conduction electrons to nematicity also encodes the coupling to nematic fluctuations that forms the pairing glue.

Here we introduce a transport coefficient that directly measures the coupling of nematicity to conduction electrons, the *spontaneous* elastoresistivity coefficient, m_S , defined as the ratio of the spontaneous resistivity anisotropy to the spontaneous structural distortion below a phase transition. Whereas $2m_{66}$ measures the linear response due to the externally applied strain, m_S plays the same role as the anomalous Hall coefficient in a ferromagnet, which measures the coupling between conduction electrons and a $q = 0$ thermodynamic order parameter. Since m_S is defined within the broken symmetry phase, its zero-temperature limit reflects the ground state properties. For example, the doping dependence of m_S near the putative quantum critical point may reveal the transport anomaly in the broken symmetry side of the phase diagram, a region that has been rarely explored in the past^{14,15}.

In this work, we introduce a method that precisely determines the spontaneous elastoresistivity coefficient by combining resistivity and x-ray diffraction measurement with in-situ tunable uniaxial stress. We show that the spontaneous elastoresistivity coefficient in the underdoped iron pnictide is a temperature independent quantity with a value equal to the value of $2m_{66}$ at the nematic transition temperature T_S . In the framework of the Landau free energy model, this equality is a direct confirmation that the proportional constant k is invariant across the phase transition. This equality also leads to an important consequence: in Figure 1, we show the values of $2m_{66}$ at the nematic transition temperature

T_S across the underdoped side of the Co-doping phase diagram. The evolution towards optimal superconductivity coincides with a nearly fourfold enhancement of the value of $2m_{66}(T_S)$, which suggests that the spontaneous elastoresistivity also increases by nearly fourfold near the optimal doping. Our study reveals a new aspect of metallic quantum criticality with implications to high- T_c superconductivity, namely that the coupling between static order and conducting electrons is enhanced as the quantum critical point is approached from the ordered side.

Precision Detwinning of Orthorhombic Domains

The main experimental challenge for a precise determination of the spontaneous elastoresistivity coefficient is the presence of orthorhombic twin domains, which cause transport measurements to average over the resistivities of the domains. Previous experiments detwinned samples using constant uniaxial stress via a clamp or constant uniaxial strain via a horseshoe device^{9,16–21}, which revealed large transport anisotropies in the ordered state maintained down to the superconducting transition or base temperature. However, the large stresses induced by these devices inevitably result in additional lattice distortions, especially in the neighborhood of the structural transition where the elastic modulus softens^{4,22,23}, obscuring the distinction between the spontaneous elastoresistivity coefficient (m_s) and the additional strain-induced resistivity anisotropy measured by the normal elastoresistivity coefficient ($2m_{66}$). More recently, the spontaneous resistivity anisotropy has been measured by the quantum gas imaging technique²⁴. Another attempt to get around this issue is a pioneering work by Tanatar et al¹⁷, in which the resistivity of an FeSe sample was measured in two tensile strain states within the nematic phase. The resistivity anisotropy was then estimated by linear extrapolation. The validity of this method relies on two assumption: the strain measured from the detwin device is a true measure of the actual lattice distortion of the crystal, and the elastoresistivity is a linear function of strain. As we shall discuss below, neither of these assumptions holds near the phase transition.

We overcome these challenges by developing a new experimental platform that combines x-ray diffraction (XRD) and electrical transport with *in-situ* uniaxial stress tunability (Fig. 2a). This platform allows us to measure the lattice constants, orthorhombic twin domain populations, and electrical resistivity simultaneously while the uniaxial stress is continuously tuned. Using this platform, we detwin a sample of $x = 0.04$ underdoped $Ba(Fe_{1-x}Co_x)_2As_2$ and extract the spontaneous resistivity anisotropy ($\eta_0 = \frac{\rho_a - \rho_b}{\rho_a + \rho_b}$) and the zero-stress structural orthorhombicity ($\varepsilon_0 = \frac{a-b}{a+b}$) within the nematic phase. The sample we use in this work is located in the underdoped side of the phase diagram with $T_S = 74K$, $T_N = 64K$ and $T_C = 74K$ (Fig. 1). We focus on the 10K range below T_S but above T_N because the long-range antiferromagnetic order reconstructs the Fermi surface and induces additional resistivity anisotropy effects^{25–28}. The key to this experiment is a uniaxial strain device²⁹ fully integrated with the beamline 6-ID-B, at the Advanced Photon Source (Fig. 2a) (see Methods). The lattice constants along the $[1\ 1\ 0]_T$, $[-1\ 1\ 0]_T$ and $[0\ 0\ 1]_T$ directions of the orthorhombic unit cell are determined from measuring the $(2\ 2\ 12)_T$, $(-1\ 1\ 14)_T$ and $(0\ 0\ 14)_T$ reflections in the tetragonal basis. The sample is oriented such that applied strain can detwin the sample and enhance the orthorhombicity. The nominal strain is defined as $\varepsilon_{xx}^{nom} = \frac{\Delta L}{L_0}$, where L_0 is the size of the gap between two titanium plates on which the sample was glued with Stycast epoxy. The displacement ΔL was determined from a capacitance strain gauge. The four-wire electrical contact geometry enables the simultaneous resistance measurements along the strain axis.

Upon cooling the sample below 74K, the single peak of the $(2\ 2\ 12)_T$ reflection splits into two peaks corresponding to the a_A and b_B orthorhombic lattice constants of the A and B domains, respectively, indicating the formation of nematic twin domains (Fig. 2a-b). Figure 2c-f shows detwinning results for a representative temperature 8K below T_S . The peak positions and intensities (I_A and I_B) are shown in Figure 2c. The relative volume fraction of the A domain is determined as $D_A(\%) = \left(\frac{I_A}{I_A + I_B} \right) \times 100$, which varies smoothly with applied stress between 0% and 100% i.e. between the B and

A monodomains (Fig. 2e, right). While the sample is mostly detwinned over a relatively small strain range, the last 10% volume fraction of the minor domain appears to persist up to large strain values. Strain homogeneity is confirmed by a nearly-constant Bragg peak width throughout the nominal strain range (Fig. 2d). A video of the XRD detwinning data is available online.

The B_{2g} orthorhombicity within a domain is defined using lattice constants along both the $[1\ 1\ 0]_T$ and $[-1\ 1\ 0]_T$ directions as $\varepsilon = \frac{a_A - b_A}{a_A + b_A}, \frac{a_B - b_B}{a_B + b_B}$ under tension and compression, respectively. A precise measurement of the spontaneous orthorhombicity ε_0 within the nematic phase near zero nominal strain can be made using the split $(2\ 2\ 12)_T$ reflection as is often done for a freestanding crystal³⁰, with $\varepsilon_0 = \frac{a_A - b_B}{a_A + b_B}$ (Fig. 2c). We observe that ε_0 is nearly constant for D_A values between 10% and 90%, leading us to define this nominal strain range as the twin domain region (Fig. 2f, between grey bars). For larger nominal strains, the crystal is mostly detwinned to a monodomain, and the induced orthorhombicity increases dramatically with increasing tensile or compressive strain. Uniaxial stress then appears to be unable to remove the last 10% of the minor domain without changing the lattice constants of the major domain. Therefore, we find that we can mostly, but not fully, detwin the sample without inducing additional lattice distortions, which warrants consideration for the design and interpretation of future experiments involving the application of uniaxial stress to detwin orthorhombic domains.

The spontaneous resistivity anisotropy η_0 results from the resistivities of the distortion-free orthorhombic domain, ρ_a and ρ_b . Under large stress, the resistivity anisotropy is rapidly enhanced due to the elasto-resistance effect of the monodomain orthorhombic crystal. In the low-stress twin domain region, the orthorhombicity is nearly constant and so we ascribe changes of resistivity to biasing the domain populations and not to elasto-resistance effects. Due to the network of twin domains running at 45° to the length of the sample³¹, the current takes nontrivial paths, with a preference for the lower-resistivity A domain, and so ρ_{xx} has a nonlinear response to D_A (Fig. 3a). Since the direct measurement of resistivity of a fully-detwinned zero-stress monodomain sample is not possible due to the persistence of the minor

domain, we determine η_0 at each temperature from the resistivities at the edges between the twin and monodomain regions, with $\rho_a = \rho_{xx}(D_A = 90\%)$ and $\rho_b = \rho_{xx}(D_A = 10\%)$ (Fig. 3b filled circles). Alternative choices within the twin domain region ($D_A = 15\%/85\%$) and in the elastoresistive strain range ($D_A = 5\%/95\%$) provide an under/over estimate of η_0 (grey/open circles).

The spontaneous resistivity anisotropy η_0 and the spontaneous orthorhombicity ε_0 are well fitted by $(T_s - T)^{\frac{1}{2}}$ (Fig. 3c-d). From the shared temperature dependence, we find that the ratio $m_s = \frac{\eta_0}{\varepsilon_0}$, i.e. the spontaneous elastoresistivity coefficient, has a temperature-independent value of $m_s \cong 155$ (135-195 for under/overestimate). The large value of m_s is consistent with previous uniaxial stress detwinned measurements, which revealed a resistivity anisotropy orders of magnitude larger than the orthorhombicity. Intriguingly, while the resistivity anisotropy is expected by symmetry to be linearly proportional to the primary nematic order parameter ψ in the infinitesimal limit ($\eta = k \psi$), the clear mean-field behavior of η_0 gives strong evidence that this linear relation is valid within the nematic phase even for large values of the order parameter (40% of the $T = 0K$ saturated value)³², with a temperature independent proportionality constant k .

To gain more insight into the physical interpretation of m_s , we examine the Landau free energy that describes a nematic phase transition with a bilinear coupling to the lattice (a full derivation presented in the methods section):

$$F = \frac{a_0(T - T^*)}{2}\psi^2 + \frac{b}{4}\psi^4 + \frac{C_{66,0}}{2}\varepsilon^2 - \lambda\psi\varepsilon$$

Here, T^* is the bare nematic transition temperature and $C_{66,0}$ is the bare elastic shear modulus^{4,22,33}, i.e. the elastic modulus of the crystal if there is no coupling to the nematicity. The B_{2g} orthorhombicity ε is linearly coupled to the nematic order parameter ψ via the nematic-elastic coupling term $\lambda\psi\varepsilon$. In the language of pseudoproper ferroelastic transitions, ψ is the primary order parameter and ε is the secondary order parameter. Within the nematic phase and in the absence of applied stress, the nematic

order parameter develops with a mean-field temperature dependence as $\psi_0 \propto (T_S - T)^{\frac{1}{2}}$ which drives the linearly-proportional spontaneous orthorhombicity ε_0 . As the two order parameters have the same temperature dependence, their temperature independent ratio is $\frac{\psi_0}{\varepsilon_0} = \frac{C_{66,0}}{\lambda}$. Physically, the magnitude of ε_0 is determined by the softness of the bare shear modulus $C_{66,0}$ and the strength of the nematic elastic coupling λ . As k and $\lambda/C_{66,0}$ are the proportionality constants of η_0 (resistivity anisotropy) and ε_0 (structural orthorhombicity) to the primary nematic order parameter ψ_0 , respectively, the spontaneous elastoresistivity coefficient $m_s = \frac{\eta_0}{\varepsilon_0}$ can also be considered as the ratio of the nematic coupling to the conduction electrons and to the lattice, $m_s = \frac{k}{(\lambda/C_{66,0})}$.

With this result, we now show that the spontaneous elastoresistivity coefficient can be obtained *without* measurements below the phase transition by analyzing the corresponding quantity in the disordered phase, the normal elastoresistivity coefficient $2m_{66} = \frac{d\eta}{d\varepsilon}$. The $2m_{66}$ coefficient is proportional to the nematic susceptibility $\chi_N = \frac{d\psi}{d\varepsilon}$, i.e. $2m_{66} = k\chi_N \propto (T - T^*)^{-1}$, which has a Curie-Weiss temperature dependence *above* the phase transition^{2,6,7}. Interestingly, the Weiss temperature corresponds to the bare nematic transition temperature T^* , which is lower than the actual phase transition temperature T_S . As nematic fluctuations diverge towards T^* , the linear coupling to the lattice effectively softens the shear modulus to zero at T_S which induces the structural transition at this higher temperature. Thus, the crystal lattice provides a polarizable medium that enhances the nematic instability. At the transition, the nematic susceptibility attains a finite value $\chi_N(T_S) = \frac{C_{66,0}}{\lambda}$, which is exactly the same value of the ratio $\frac{\psi_0}{\varepsilon_0}$ maintained below the phase transition. Therefore, the softer the bare shear modulus $C_{66,0}$ and the stronger the nematic elastic coupling λ , the smaller the χ_N is required to satisfy the phase transition condition. From this equality of thermodynamic quantities, $\frac{\psi_0}{\varepsilon_0} = \chi_N(T_S)$, we deduce that the

equality also holds for the corresponding transport coefficients, $m_s = 2m_{66}(T_S)$, if the constant k is invariant *across* the phase transition.

In Figure 3e, we compare our measurement of m_s to $2m_{66}$ for a second sample from the same growth batch measured using the standard modified Montgomery measurement². The $2m_{66}$ data follows a Curie-Weiss fit over a range 100K-200K, with $R^2 > 0.99$. Between 80K and 100K (note the slightly higher transition temperature, $T_S = 79.5K$) the value is sub-Curie Weiss, as is commonly found for dopings near the optimal doping. We find that the measured value of 128 and the high temperature fit value of 148 of $2m_{66}(T_S)$ fall within our estimated range of m_s . The agreement between m_s and $2m_{66}(T_S)$ confirms that the proportionality of nematicity to resistivity anisotropy (k) is essentially unchanged through the phase transition, and so the resistivity anisotropy remains a valid proxy of the nematicity above, below and through the transition.

Nematic Fluctuation Softening of the Shear Modulus

Finally, we independently verify the equality $\chi_N(T_S) = \frac{C_{66,0}}{\lambda}$ by analyzing the temperature dependence of the shear modulus C_{66} , which can be extracted from the lattice response to uniaxial stress. The temperature dependence of C_{66} emerges from the second derivative of the Landau free energy with respect to strain, as $C_{66} = C_{66,0} - \lambda\chi_N$. Therefore, we expect C_{66} to also show a Curie-Weiss temperature dependence and approach zero at T_S . Figure 4a shows the inline and transverse in-plane lattice constants at 74K, just above the transition temperature. Both lattice constants show a large response to strain which is dampened with increasing applied strain. The orthorhombicity likewise has an increasingly nonlinear response to strain with cooling (Fig. 4b). We define the strain transmission as $\frac{d\varepsilon_{xx}}{d\varepsilon_{xx}^{nom}}$ and the in-plane Poisson ratio as $\nu_{xy} = -\frac{d\varepsilon_{yy}}{d\varepsilon_{xx}}$, where ε_{xx} , $\varepsilon_{yy} = \frac{\Delta L}{L_0}$ are the XRD-measured strains of the inline and transverse lattice constants, respectively. In Figure 4c, a large enhancement of strain transmission occurs with cooling, approaching 95% at T_S . The application of tensile and compressive stress

stiffens the sample and the strain transmission returns to a baseline ~40%-50% value. The Poisson ratio also shows similar behavior (Fig. 4d): under zero stress, ν_{xy} approaches 1 with cooling to T_S and decreases even faster with increasing nominal strain. All these effects can be understood in terms of the shear modulus C_{66} approaching zero at T_S and the stiffening of C_{66} as applied strain tunes the system away from the critical point.

We extract the shear modulus from the zero-stress value of the Poisson ratio using $C_{66} = (50.5 \text{ GPa}) \frac{1-\nu_{xy}}{1+\nu_{xy}}$, where the magnitude is determined from other elastic modulus terms using ultrasound data from ref.²² (see supplementary materials). In Figure 4e, we observe C_{66} diminishes to nearly zero at T_S . The Curie-Weiss fitted temperature dependence (red line) yields a fitted value of the bare shear modulus $C_{66,0} = 38.8 \pm 4.7 \text{ GPa}$ in agreement with the high-temperature ultrasound data²². The extracted $T_S - T^* = 23.8 \text{ K} \pm 8.3 \text{ K}$ agrees with the Curie-Weiss fitted value for the $2m_{66}$ data presented in Figure 3e of $T_S - T^* = 28 \text{ K} \pm 0.5 \text{ K}$; however, this is considerably smaller than the value obtained from several other shear modulus measurements^{33,34}, where $T_S - T^* \sim 40 \text{ K} - 50 \text{ K}$. Puzzlingly, a variety of such measurements have not observed the shear modulus to drop to zero at the transition as is expected. In our measurement the Poisson ratio diverges to 1 at T_S , and so our measured quantity has its largest value at the transition itself. From this result, we can conclude that the nematic susceptibility follows a Curie-Weiss temperature dependence up to the transition temperature and attains a value at T_S of $\chi_N(T_S) = \frac{C_{66,0}}{\lambda}$.

Discussion and Conclusion

We now return to the doping dependence of $2m_{66}(T_S)$ shown in Figure 1, which not only indicates that nematic fluctuations themselves are enhancing but also that the direct coupling of nematicity to conduction electrons is enhancing. Thus, even though the size of the thermodynamic order parameter vanishes as the system is tuned close to the quantum phase transition, the conduction electrons at the

Fermi surface become increasingly sensitive to the orthorhombic distortion. Such an enhancement has been inferred from previous measurements of $2m_{66}$ in the same material system^{3,18}. In this work we clearly establish the correspondence of $2m_{66}(T_S)$ to the ordered phase quantity, the spontaneous elastoresistivity coefficient m_S , and provide a direct physical explanation; **the ratio between the symmetry breaking transport coefficient and the thermodynamic order parameter enhances on approach to the critical point, suggesting that the sensitivity of conduction electrons to the lattice orthorhombicity enhances with doping even as the nematic order is suppressed.** The observation of an enhanced value of $2m_{66}(T_S)$ near the nematic quantum critical point of $\text{FeSe}_{1-x}\text{S}_x$ ⁶ and $\text{LaFe}_{1-x}\text{Co}_x\text{AsO}$ ⁷ and large stressed induced optical anisotropy in optimally doped $\text{Ba}_{0.6}\text{K}_{0.4}\text{Fe}_2\text{As}_2$ ³⁵ indicates that this is generic to several families of iron-based superconductors.

From the experimental perspective, the use of x-ray diffraction gives unprecedented detail in the detwinning process itself and reveals a highly non-linear structural response close to the phase transition. While similar uni-axial stress approaches have been used recently to explore interesting properties in iron pnictides and beyond^{36–44}, this work highlights the importance of in-situ microscopic measurement of structurally-complex quantum materials.

Methods (end of document)

Acknowledgments: We thank Cenke Xu, Jing-Yuan Chen, and Matthias Ikeda for discussion. **Funding:**

This work was mainly supported by NSF MRSEC at UW (DMR-1719797) and the Air Force Office of Scientific Research Young Investigator Program under Grant FA9550-17-1-0217. J.H.C. acknowledge the support of the Gordon and Betty Moore Foundation’s EPIQS Initiative, Grant GBMF6759 to J.-H.C, the David and Lucile Packard Foundation, the Alfred P. Sloan foundation and the State of Washington funded Clean Energy Institute. J. L. acknowledges support from the National Science Foundation under

Grant No. DMR-1848269. This research used resources of the Advanced Photon Source, a U.S. Department of Energy (DOE) Office of Science User Facility operated for the DOE Office of Science by Argonne National Laboratory under Contract No. DE-AC02-06CH11357. J.J.S. was partially supported by the U.S. Department of Energy, Office of Science, Office of Workforce Development for Teachers and Scientists, Office of Science Graduate Student Research (SCGSR) program, administered by the Oak Ridge Institute for Science and Education (ORISE) for the DOE. ORISE is managed by ORAU under contract number DE-SC0014664.

Author contributions: J.M. grew the samples. J.J.S. and P.M. did the experiments. P.R., J.-W.K., and J.L. helped conceive and design the XRD measurements at the APS. J.J.S. analyzed the data. J.H.C. supervised the project. All authors contributed extensively to the interpretation of the data and the writing of the manuscript.

Competing interests: Authors declare no competing interests.

References

1. Fradkin, E., Kivelson, S. A., Lawler, M. J., Eisenstein, J. P. & Mackenzie, A. P. Nematic Fermi Fluids in Condensed Matter Physics. *Annu. Rev. Condens. Matter Phys.* **1**, 153–178 (2010).
2. Kuo, H. H., Chu, J. H., Palmstrom, J. C., Kivelson, S. A. & Fisher, I. R. Ubiquitous signatures of nematic quantum criticality in optimally doped Fe-based superconductors. *Science*. **352**, 958–962 (2016).
3. Chu, J.-H., Kuo, H.-H., Analytis, J. G. & Fisher, I. R. Divergent Nematic Susceptibility in an Iron Arsenide Superconductor. *Science*. **337**, 710–71 (2012).
4. Böhmer, A. E. & Meingast, C. Electronic nematic susceptibility of iron-based superconductors. *Comptes Rendus Phys.* **17**, 90–112 (2016).
5. Kuo, H.-H., Shapiro, M. C., Riggs, S. C. & Fisher, I. R. Measurement of the elastoresistivity coefficients of the underdoped iron arsenide BaFe_2As_2 . *Phys. Rev. B* **88**, 85113 (2013).
6. Hosoi, S. *et al.* Nematic quantum critical point without magnetism in $\text{FeSe}_{1-x}\text{S}_x$ superconductors. *Proc. Natl. Acad. Sci. U. S. A.* **113**, 8139–8143 (2016).
7. Hong, X. C. *et al.* Evolution of the nematic susceptibility in $\text{LaFe}_{1-x}\text{Co}_x\text{AsO}$. (2019).
8. Shapiro, M. C., Hristov, A. T., Palmstrom, J. C., Chu, J. & Fisher, I. R. Measurement of the B_{1g} and B_{2g} components of the elastoresistivity tensor for tetragonal materials via transverse resistivity configurations. *Rev. Sci. Instrum.* **063902**, (2016).
9. Ishida, S. *et al.* Anisotropy of the In-Plane Resistivity of Underdoped $\text{Ba}(\text{Fe}_{1-x}\text{Co}_x)_2\text{As}_2$ Superconductors Induced by Impurity Scattering in the Antiferromagnetic Orthorhombic Phase. *Phys. Rev. Lett.* **110**, 207001 (2013).
10. Gastiasoro, M. N., Paul, I., Wang, Y., Hirschfeld, P. J. & Andersen, B. M. Emergent defect states as a source of resistivity anisotropy in the nematic phase of iron pnictides. *Phys. Rev. Lett.* **113**, 127001 (2014).
11. Fernandes, R. M., Abrahams, E. & Schmalian, J. Anisotropic in-plane resistivity in the nematic phase of the iron pnictides. *Phys. Rev. Lett.* **107**, 217002 (2011).
12. Kuo, H. H. & Fisher, I. R. Effect of disorder on the resistivity anisotropy near the electronic nematic phase transition in pure and electron-doped BaFe_2As_2 . *Phys. Rev. Lett.* **112**, 227001 (2014).
13. Lederer, S., Schattner, Y., Berg, E. & Kivelson, S. A. Enhancement of superconductivity near a nematic quantum critical point. *Phys. Rev. Lett.* **114**, 097001 (2015).
14. Analytis, J. G. *et al.* Transport near a quantum critical point in $\text{BaFe}_2(\text{As}_{1-x}\text{P}_x)_2$. *Nat. Phys.* **10**, 194–197 (2014).
15. Hayes, I. M. *et al.* Scaling between magnetic field and temperature in the high-temperature superconductor $\text{BaFe}_2(\text{As}_{1-x}\text{P}_x)_2$. *Nat. Phys.* **12**, 916–919 (2016).
16. Tanatar, M. A. *et al.* Uniaxial-strain mechanical detwinning of CaFe_2As_2 and BaFe_2As_2 crystals: Optical and transport study. *Phys. Rev. B - Condens. Matter Mater. Phys.* **81**, 184508 (2010).
17. Tanatar, M. A. *et al.* Origin of the Resistivity Anisotropy in the Nematic Phase of FeSe . *Phys. Rev. Lett.* **117**, 127001 (2016).
18. Chu, J. In-Plane Resistivity Anisotropy in an Underdoped Iron Arsenide Superconductor. *Science*. **329**, 824–826 (2010).
19. Liu, L. *et al.* In-plane electronic anisotropy in the antiferromagnetic orthorhombic phase of isovalent-substituted $\text{Ba}(\text{Fe}_{1-x}\text{Ru}_x)_2\text{As}_2$. *Phys. Rev. B* **92**, 094503 (2015).
20. Blomberg, E. C. *et al.* In-plane anisotropy of electrical resistivity in strain-detwinned SrFe_2As_2 . *Phys. Rev. B* **83**, 134505 (2011).
21. Fisher, I. R., Degiorgi, L. & Shen, Z. X. In-plane electronic anisotropy of underdoped ‘122’ Fe-

- arsenide superconductors revealed by measurements of detwinned single crystals. *Reports Prog. Phys.* **74**, 124506 (2011).
22. Fujii, C. *et al.* Anisotropic Grüneisen Parameter and Diverse Order Parameter Fluctuations in Iron-Based Superconductor $\text{Ba}(\text{Fe}_{1-x}\text{Co}_x)_2\text{As}_2$. *J. Phys. Soc. Japan* **87**, 074710 (2018).
 23. Fernandes, R. M. *et al.* Effects of Nematic Fluctuations on the Elastic Properties of Iron Arsenide Superconductors. *Phys. Rev. Lett.* **105**, 157003 (2010).
 24. Yang, F. *et al.* Nematic transitions in iron pnictide superconductors imaged with a quantum gas. *Nat. Phys.* 1–6 (2020). doi:10.1038/s41567-020-0826-8
 25. Analytis, J. G. *et al.* Quantum oscillations in the parent pnictide BaFe_2As_2 : Itinerant electrons in the reconstructed state. *Phys. Rev. B - Condens. Matter Mater. Phys.* **80**, 064507 (2009).
 26. Shimojima, T. *et al.* Orbital-Dependent modifications of electronic structure across the magnetostructural transition in BaFe_2As_2 . *Phys. Rev. Lett.* **104**, 057002 (2010).
 27. Nakajima, M. *et al.* Unprecedented anisotropic metallic state in undoped iron arsenide BaFe_2As_2 revealed by optical spectroscopy. *Proc. Natl. Acad. Sci. U. S. A.* **108**, 12238–12242 (2011).
 28. Watson, M. D. *et al.* Probing the reconstructed Fermi surface of antiferromagnetic BaFe_2As_2 in one domain. *npj Quantum Mater.* **4**, 1–9 (2019).
 29. Hicks, C. W., Barber, M. E., Edkins, S. D., Brodsky, D. O. & Mackenzie, A. P. Piezoelectric-based apparatus for strain tuning. *Rev. Sci. Instrum.* **85**, 065003 (2014).
 30. Kim, M. G. *et al.* Character of the structural and magnetic phase transitions in the parent and electron-doped BaFe_2As_2 compounds. *Phys. Rev. B* **83**, 134522 (2011).
 31. Tanatar, M. A. *et al.* Direct imaging of the structural domains in the iron pnictides AFe_2As_2 ($\text{A}=\text{Ca}, \text{Sr}, \text{Ba}$). *Phys. Rev. B - Condens. Matter Mater. Phys.* **79**, 1–4 (2009).
 32. Carlson, E. W., Dahmen, K. A., Fradkin, E. & Kivelson, S. A. Hysteresis and noise from electronic nematicity in high-temperature superconductors. *Phys. Rev. Lett.* **96**, 097003 (2006).
 33. Yoshizawa, M. *et al.* Structural Quantum Criticality and Superconductivity in Iron-Based Superconductor $\text{Ba}(\text{Fe}_{1-x}\text{Co}_x)_2\text{As}_2$. *J. Phys. Soc. Japan* **81**, 024604 (2012).
 34. Böhmer, A. E. *et al.* Nematic Susceptibility of Hole-Doped and Electron-Doped BaFe_2As_2 Iron-Based Superconductors from Shear Modulus Measurements. *Phys. Rev. Lett.* **112**, 047001 (2014).
 35. Pal, A. *et al.* Optical anisotropy in optimally doped iron-based superconductor. *npj Quantum Mater.* **4**, 1–5 (2019).
 36. Schmidt, J. *et al.* Nematicity in the superconducting mixed state of strain detwinned underdoped $\text{Ba}(\text{Fe}_{1-x}\text{Co}_x)_2\text{As}_2$. *Phys. Rev. B* **99**, 064515 (2019).
 37. Pfau, H. *et al.* Detailed band structure of twinned and detwinned BaFe_2As_2 studied with angle-resolved photoemission spectroscopy. *Phys. Rev. B* **99**, 035118 (2019).
 38. Kissikov, T. *et al.* Uniaxial strain control of spin-polarization in multicomponent nematic order of BaFe_2As_2 . *Nat. Commun.* **9**, 1058 (2018).
 39. Zheng, X. Y., Feng, R., Ellis, D. S. & Kim, Y. J. Bulk-sensitive imaging of twin domains in $\text{La}_{2-x}\text{Sr}_x\text{CuO}_4$ under uniaxial pressure. *Appl. Phys. Lett.* **113**, 071906 (2018).
 40. Kim, H. H. *et al.* Uniaxial pressure control of competing orders in a high-temperature superconductor. *Science*. **362**, 1040–1044 (2018).
 41. Ikeda, M. S. *et al.* Symmetric and antisymmetric strain as continuous tuning parameters for electronic nematic order. *Phys. Rev. B* **98**, 1–6 (2018).
 42. Malinowski, P. *et al.* Drastic suppression of superconducting T_c by anisotropic strain near a nematic quantum critical point. (2019).
 43. Dhital, C. *et al.* Effect of uniaxial strain on the structural and magnetic phase transitions in BaFe_2As_2 . *Phys. Rev. Lett.* **108**, 087001 (2012).
 44. Lu, X. *et al.* Nematic spin correlations in the tetragonal state of uniaxial-strained $\text{BaFe}_{2-x}\text{Ni}_x\text{As}_2$. *Science*. **345**, 657–660 (2014).

45. Palmstrom, J. C. *et al.* Comparison of temperature and doping dependence of nematic susceptibility near a putative nematic quantum critical point. (2019).
46. Chu, J. H., Analytis, J. G., Kucharczyk, C. & Fisher, I. R. Determination of the phase diagram of the electron-doped superconductor $\text{Ba}(\text{Fe}_{1-x}\text{Co}_x)_2\text{As}_2$. *Phys. Rev. B* **79**, (2009).

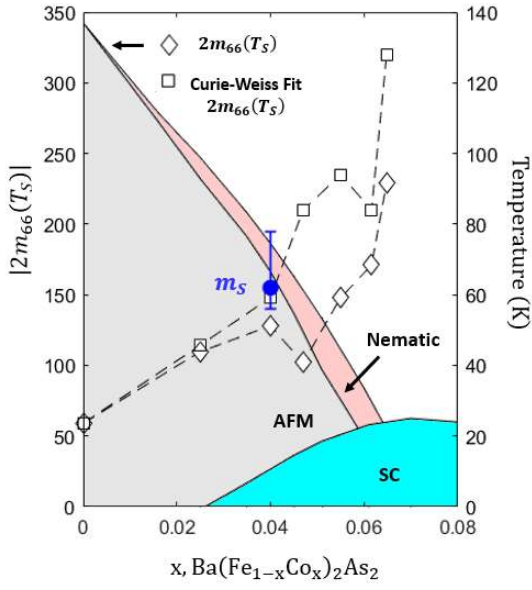


Figure 1 | : x - T phase diagram of Co-doped BaFe_2As_2 . The value of the elastoresistivity coefficient $2m_{66}$ at the nematic transition T_S shows an enhancing magnitude towards optimal doping ($x=0.067$) for both the measured value (diamonds) and for the high-temperature Curie-Weiss fit value (squares) (see Fig. 3e). The spontaneous elastoresistivity coefficient m_S (blue) evaluated within the nematic phase is in agreement with $2m_{66}(T_S)$ values. $2m_{66}$ data for $x=0, 0.025, 0.047, 0.053$ from ref. ², for $x=0.616$ and 0.0648 from ref. ⁴⁵, and for $x=0.04$ from the present work.

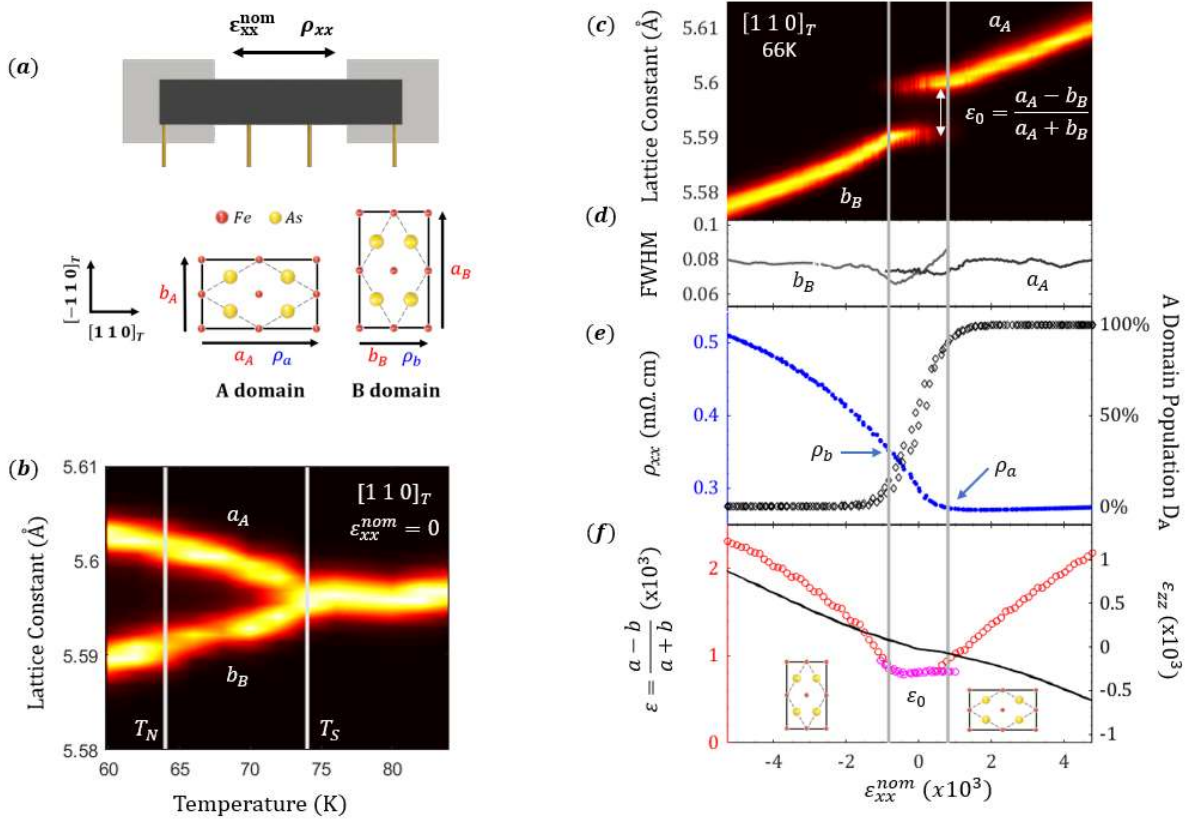


Figure 2 | X-ray diffraction of domain detwinning. (a) Schematic of the sample measurement geometry and strain device. Uniaxial stress is applied along the tetragonal $[1\ 1\ 0]_T$ direction. Inline resistivity ρ_{xx} measures ρ_a of the A domain and ρ_b of the B domain. (b) Zero-stress x-ray diffraction of the $(2\ 2\ 12)_T$ reflection yields the lattice constants aligned with the $[1\ 1\ 0]_T$ direction. (c-f) Detwinning results at 66K. (c) Nominal strain response of the $[1\ 1\ 0]_T$ direction lattice constants a_A and b_B with intensities I_A and I_B . (d) The full-width half maximum (FWHM) of the Gaussian fit to the XRD peak for both a_A and b_B . (e, right) Relative A domain population, $D_A = \frac{I_A}{I_A + I_B}$. Grey bars across figure show $D_A = 10\%$ and $D_A = 90\%$. The small spread of D_A values near zero strain is due to variance in peak intensities from strain-shifted crystal grain orientations and not due to a detwinning hysteresis (see supplementary materials). (e, left) Inline resistivity with estimates of the resistivities ρ_a and ρ_b at $D_A = 90\%$ and $D_A = 10\%$. (f, left) In-plane orthorhombicity $\varepsilon = \frac{a-b}{a+b}$ determined from within a single domain (red) or from between

the twin domains (ε_0 , magenta). (f, right) The out of plane strain $\varepsilon_{zz} = \frac{\Delta c}{c_0}$, which shows a flattened response in the detwinning strain regime.

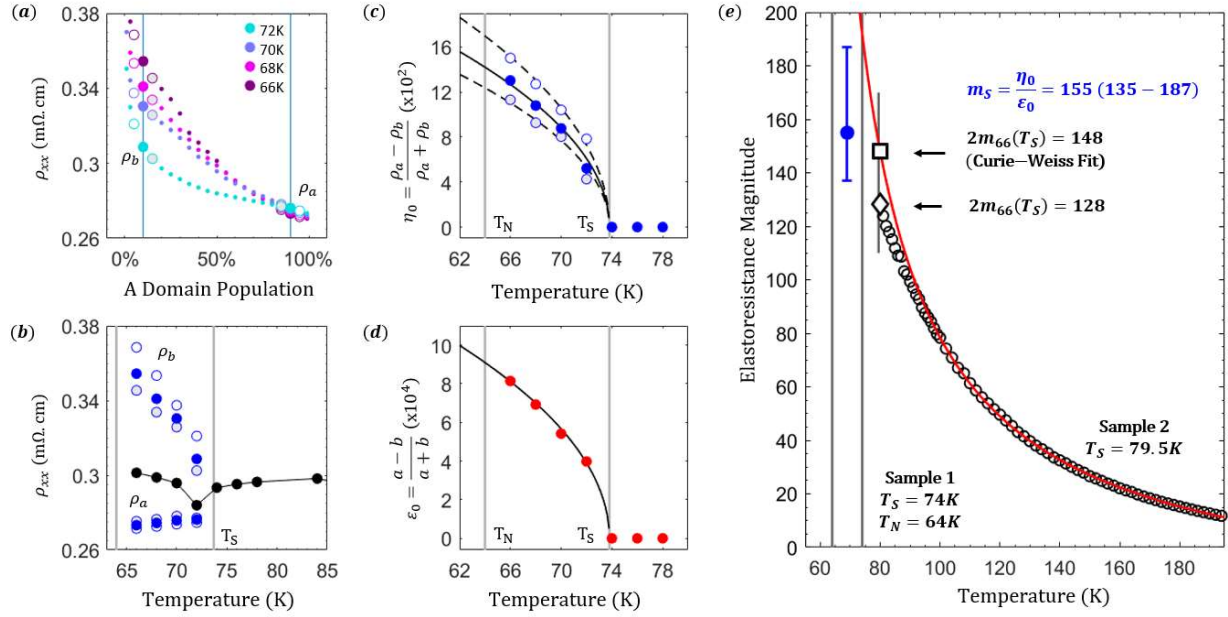


Figure 3 | Spontaneous Elasto-resistivity Coefficient. (a) Resistivity ρ_{xx} as a function of A domain population at 4 temperatures within the nematic phase. The zero-stress monodomain resistivities ρ_a and ρ_b are extracted from the 10% and 90% D_A points (filled circles), with an under-over estimate taken at the 15%/85% and 5%/95% D_A points (grey/white circles). (b) The values of ρ_a and ρ_b below the transition and the measured ρ_{xx} at the zero nominal strain point (black). (c-d) The spontaneous resistivity anisotropy η_0 and the spontaneous orthorhombicity ε_0 within the nematic phase. Both quantities are well fit to a $(T_S - T)^{\frac{1}{2}}$ temperature dependence with $T_S = 73.8K$ and $R^2=0.97$ and 0.99 respectively, indicating that both are proportional to a mean-field nematic ordering. (e) The spontaneous elasto-resistivity coefficient is determined from the ratio of the fits to η_0 and ε_0 as $m_S = \frac{\eta_0}{\varepsilon_0} = 155$ (135-187) (blue). The $2m_{66}$ elasto-resistivity coefficient was measured for a second sample (black circles) in the disordered phase. At the second sample's nematic transition temperature, $T_S = 79.5K$, both the measured value (diamond) and high-temperature Curie-Weiss fit value (square) are within or close to the estimated range of the spontaneous elasto-resistivity coefficient.

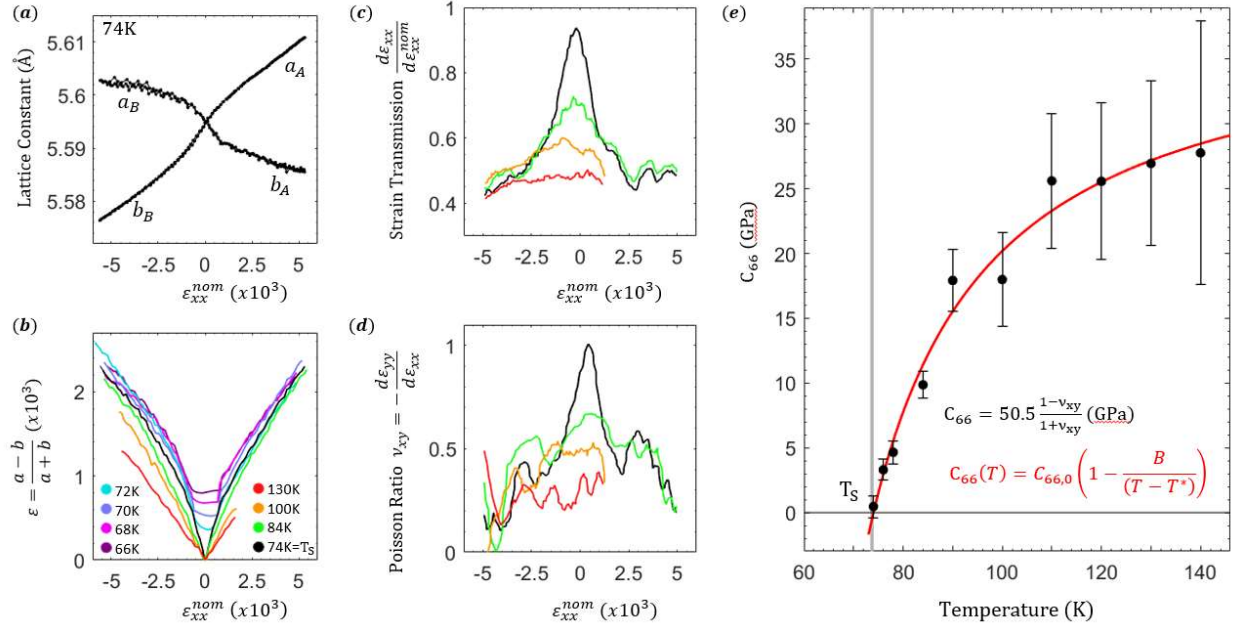


Figure 4 | Nematic fluctuation softening of the shear modulus. (a) In-plane lattice constants vs strain at $T = 74K$, concurrent with the structural transition. Within the disordered phase we refer to the strain-induced A and B domains as we do the spontaneous domains below the transition. (b) In-plane orthorhombicity vs nominal strain above and below the transition. (c) The strain transmission $\frac{d\epsilon_{xx}}{d\epsilon_{xx}^{nom}}$ and (d) in-plane Poisson ratio $\nu_{xy} = -\frac{d\epsilon_{yy}}{d\epsilon_{xx}}$ vs nominal strain. We define $\epsilon_{xx} = \frac{\Delta L}{L_0}$ as the strain of the lattice constant along the uniaxial stress direction ($[1\ 1\ 0]_T$), and likewise ϵ_{yy} for the in-plane transverse direction ($[-1\ 1\ 0]_T$). Both strain transmission and in-plane Poisson ratio show an enhancement near zero strain which increases with cooling to the transition. (e) Extracted shear modulus vs temperature. The shear modulus is determined from the peak value of the in-plane Poisson ratio ν_{xy} as $C_{66} = 50.5 \frac{1-\nu_{xy}}{1+\nu_{xy}}$ (GPa). Error bars represent one standard deviation (derived from the standard deviation of ν_{xy} over a small strain range 1.5×10^{-3} about the peak value of ν_{xy}). The shear modulus over a temperature range of 74K to 140K is well fitted to a Curie-Weiss temperature dependence as $C_{66}(T) =$

$C_{66,0} \left(1 - \frac{B}{(T-T^*)}\right)$, with $R^2 = 0.97$ and fit values $C_{66,0} = 38.8 \pm 4.7 \text{ GPa}$, $T^* = 50.0 \pm 8.3 \text{ K}$ and $B = 24.0 \pm 7.8 \text{ K}$.

Methods

- 1. Sample Preparation**
- 2. Determining the zero nominal strain point**
- 3. Repeatability of strain states over multiple strain loops**
- 4. Determination of the Nematic Phase Domain Population + Detwinning Video Description**
- 5. Determination of the Poisson Ratio.**
- 6. Extraction of Shear Modulus from Poisson Ratio**
- 7. Free Energy Derivation**

1. Sample Preparation

Single crystal samples of $Ba(Fe_{0.96}Co_{0.04})_2As_2$ were grown from an FeAs flux as described elsewhere⁴⁶. The primary sample used in x-ray measurements was prepared as a thin bar of dimensions 2.0 x 0.57 x 0.07 mm and cut along the Fe-Fe bonding direction. A piezo-actuator uniaxial strain device (*Razorbill Instruments, CS-100*) was used to provide in-situ strain. The nominal strain (ϵ_{xx}^{nom}) is defined as $\frac{\Delta L}{L_0}$, where $L_0=1.08$ mm is the size of the gap between two titanium plates on which the sample was glued with Stycast epoxy. The displacement ΔL was determined from sampling a capacitance strain gauge using an Andeen-Hagerling AH2550A capacitance bridge. Nominal strains of $\pm 0.5\%$ were obtainable with this setup, which was sufficient to fully detwin the sample at all temperatures. The four-wire electrical contact geometry is illustrated in Fig.2(a). Gold wires were glued with DuPont 4929 silver epoxy underneath the sample to not obstruct the x-ray diffraction off the top surface of the crystal. Measurements of the resistivity coefficient ρ_{xx} aligned along the stress axis were performed using a standard 4-point measurement and an SR830 lock-in amplifier. A second sample from the same batch was prepared as in² and the modified Montgomery method was used to determine $2m_{66}$.

X-ray diffraction (XRD) measurements were performed at the Advanced Photon Source, beamline 6-ID-B, at Argonne National Laboratories. X-rays of energy 11.215 keV illuminated an area 500x500 μ m, fully encompassing a cross section of the middle of the crystal where strain transmission is highest. The sample and strain device were mounted on a closed cycle cryostat. Gaussian fits to the tetragonal $(2\ 2\ 12)_T$, $(-1\ 1\ 14)_T$ and $(0\ 0\ 14)_T$ reflections were used to determine the orthorhombic lattice constants in the direction of applied stress (a_A & b_B), in-plane transverse to the stress (a_B & b_A) and normal to the plane (c), as labeled in Fig. 2(a).

2. Determining the zero nominal strain point

The nominal strain was determined from sampling the capacitance strain gauge as discussed above, but the capacitance value corresponding to true zero strain is temperature dependent. The differential thermal contractions between the sample and the stress device causes a thermal strain which is not captured by the strain gauge measurement, and so the room-temperature value of the capacitance strain gauge is the incorrect value to use at the temperatures of interest (66K-140K).

However, direct information on the strain state of the sample is available from x-ray diffraction (XRD) data. Our sample was initially cooled under zero voltage on the strain device, and within the nematic phase the split $(2\ 2\ 12)_T$ peak was found to have a much higher XRD intensity for the a_A peak relative to the b_B peak, indicating that it was already in a tensile state due to the differential thermal contractions. We defined the zero of the nominal strain range as the 50% A domain population point at 66K and used this as the zero-strain reference point for the temperature range of 66K-140K. In this range, this choice of zero-strain point coincides with the 50% A domain population point of the other nematic-phase temperature points (66K-72K) and also aligns with the peak in the strain transmission to the orthorhombic “a” $[1\ 1\ 0]_T$ lattice constant in the tetragonal phase (74K-140K), further increasing our confidence in this choice (Figure 3(a), main text).

Our determination of the spontaneous orthorhombicity within the nematic phase does not depend on the nominal strain measured by the capacitance strain gauge. Our analysis of the Poisson ratio and shear modulus depend as well on purely XRD data and only use the nominal strain as a reference point. Therefore the small uncertainty in nominal zero strain point across temperatures has a minimal effect on the central results of this paper.

3. Repeatability of strain states over multiple strain loops

We seek to determine the 3 orthorhombic lattice constants as a function of strain. One methodology is to measure multiple reflections while the sample is held at a single fixed nominal strain value, to ensure that all lattice constants are determined in the same strain state. However, rotating the sample and detector to reach multiple peaks at each strain step increases the time of each measurement substantially and also introduces the issue of relocating the peak intensity lineup conditions upon return to each reflection, as small misalignments can occur from repeated rotations. Therefore, at a fixed temperature we measured a single reflection and varied the strain from compressive to tensile values and back, repeating for each reflection. Any offsets in the nominal strain measured between these multiple strain loops would then introduce strain offset errors when comparing the lattice constants.

However, we believe these strain offset errors to be extremely small. Our most sensitive gauge of the attained strain state throughout the bulk of the sample is the resistivity; for instance, at 74K under compression the resistivity change to nominal strain is about a factor of 40, while the in-plane lattice constant change with nominal strain measured by XRD is about a factor of $\frac{1}{2}$. At all temperatures, the resistivity vs nominal strain curves are nearly identical for multiple sweeps of voltage on the stress device, implying repeatability of the attained strain state during the measurement of the 3 reflections (FigS1(a)).

Here we show that the nominal strain values are equivalent between multiple strain loops within the resolution of the resistivity and nominal strain measurements. We select the most strain-sensitive range of resistivity data from the 74K compressive strain regime to analyze (FigS1(b)). In this regime, the resistivity is approximately linear over small strain ranges. The deviations of resistivity to a linear fit is calculated for the three strain loops separately and for a combined data set. We perform a statistical F test on the variances of these separate and combined data sets and obtain a p-value of 0.44, indicating that from the resolution of the measurement itself we see no statistically different distribution of resistivity vs strain values between the different strain loops. Therefore, we conclude that our

measurement protocol does not introduce additional strain offset errors into our data analysis beyond the noise of the capacitance strain gauge measurement itself.

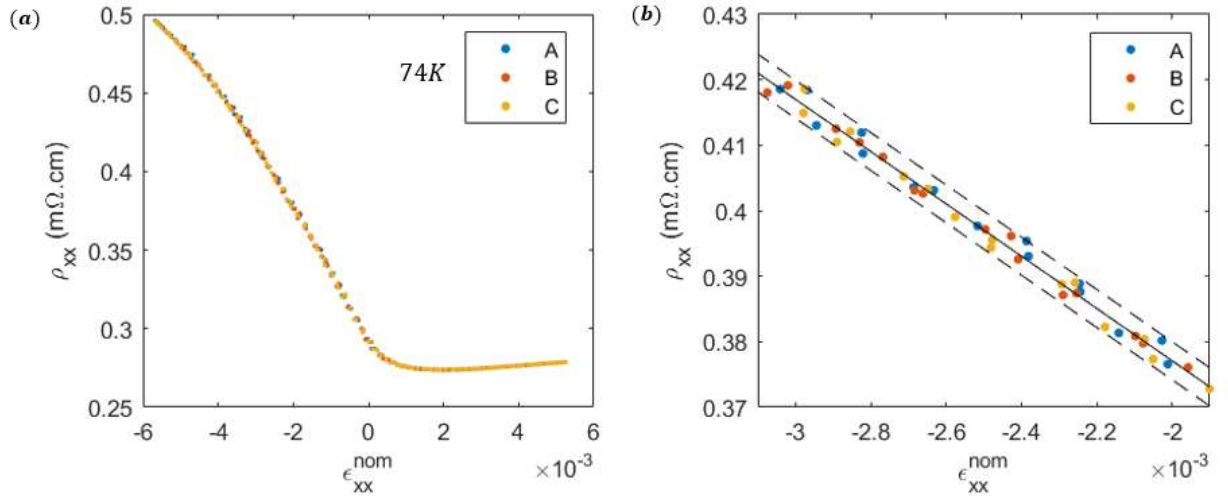


Figure S1. Resistivity vs nominal strain at 74K. A, B and C refer to separate strain loops at fixed temperature during the measurement of the $(2\ 2\ 12)_T$, $(-1\ 1\ 14)_T$ and $(0\ 0\ 14)_T$ reflections, respectively. (b) A small strain range of (a) showing the distribution of resistivity points. Solid line shows a linear fit, dashed line a 95% confidence interval for the combined dataset.

4. Determination of the Nematic Phase Domain Population

Within the nematic phase, the relative population of the A domain is defined by the intensities I_A and I_B of the a_A and b_B peaks in the $(2\ 2\ 12)_T$ reflection as $D_A(\%) = \frac{I_A}{I_A + I_B}$. In order to track the minor domain peak during detwinning, an analysis protocol was developed. First a single peak in the monodomain region was fit with a single Gaussian to determine a peak width parameter to be used for fitting the two twin domain peaks, which was roughly constant across the whole strain range. Then, at a strain point where both twin domain peaks were roughly the same intensity (implying a strain point close to the true zero strain point), the peaks were each fit to a Gaussian. After this point, changing the strain state causes one peak to increase in relative intensity while the other diminishes. At each successive strain point, the minor peak is tracked based on the fitting parameters of the previous strain point fit, so that the same peak can be effectively tracked as its intensity drops to 5% or less of its maximum value. The minor domain retains a nonzero value into the detwinned “monodomain” strain ranges where the lattice shows large stress-induced changes, likely due to pinning around defect sites.

X-ray data was taken at each fixed temperature through a strain loop from maximum compression to tension and back. Between the two sweeps, there was difference of 5%-10% in the value of the D_A within the twin domain strain region (Fig.S3(a)). At first glance, this result suggests a detwinning hysteresis. However, the resistivity data shows nearly identical values between the two directions of the strain loop, suggesting the bulk of the sample is indeed returning to the same domain configuration at each nominal strain point. Further, the direction of the offsets is actually opposite the normal hysteresis orientation, as shown by the arrows in Figure S3. Therefore, we attribute this offset to strain-induced shifts in the orientation of crystal grains causing small changes in the illuminated volume of the crystal. **We use the average of the two loops to calculate the A domain relative population for defining the twin domain boundaries ($D_A = 10\%, 90\%$).** Fortuitously, the offsets are minimal at the detwinning boundaries, and

so this feature in the data does not greatly impact our determination of the detwinned monodomain resistivities ρ_A and ρ_B .

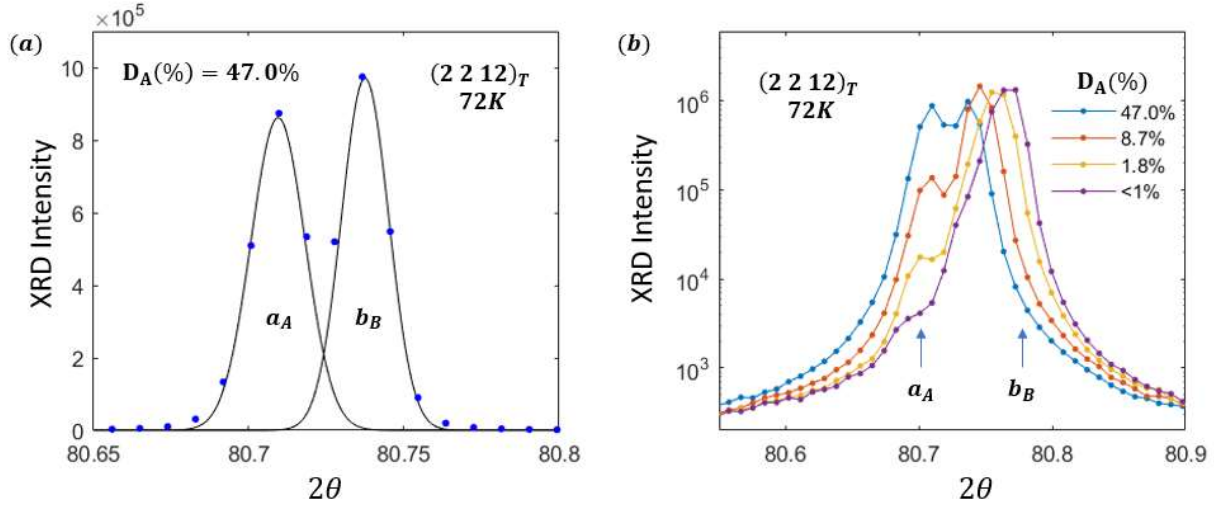


Figure S2. (a) Intensity of the $(2\ 2\ 12)_T$ reflection at 72K, just below the transition temperature ($T_S = 74K$). The split peak is fit to two Gaussians, and the fit intensities of each (I_A and I_B) are used to find the relative population of the A domain as $D_A(\%) = \frac{I_A}{I_A + I_B}$. (b) Log scale intensity of the suppression of I_A with compression. Lines are a guide to the eye.

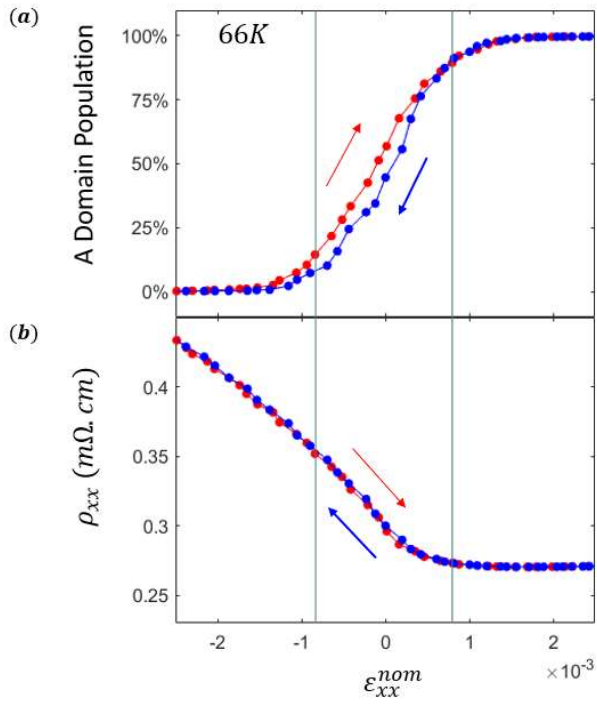


Figure S3. (a) The A domain population and (b) the resistivity during detwinning along the tensioning (red) and compressing (blue) strain sweeps. Grey bars show the 10% and 90% A domain population points.

Domain Detwinning Video 66K

A video of the detwinning process at 66K is available online, as strain is applied through a loop from maximum compression to maximum tension and back.

Top plot: Log-scale intensities of the split $(2\ 2\ 12)_T$ peak across the whole area detector (chi vs 2θ).

Middle plot: Gaussian fits to the chi-summed intensity vs 2θ .

Bottom plot: Relative amplitudes of the Gaussian fits yields the relative population of the A domain

$$(D_A = \frac{I_A}{I_A + I_B} \times 100).$$

5. Determination of the Poisson Ratio.

We define our coordinate system with the x, y and z axes aligned to the tetragonal $[1\ 1\ 0]_T$, $[-1\ 1\ 0]_T$ and $[0\ 0\ 1]_T$ directions as in Figure 2(a) of the main text. In this section we restrict our focus to the tetragonal phase ($T > T_S$) in which there are no twin domains, and we will refer to the lattice constants aligned with the $[1\ 1\ 0]_T$, $[-1\ 1\ 0]_T$ and $[0\ 0\ 1]_T$ direction as "a", "b", and "c" respectively.

Uniaxial stress is applied along the x-axis, which induces a strain $\varepsilon_{xx} = \frac{\Delta a}{a_0}$. Any x-axis strain induces transverse direction strains given by the Poisson ratios $\nu_{xy} = -\frac{\varepsilon_{yy}}{\varepsilon_{xx}}$ and $\nu_{xz} = -\frac{\varepsilon_{zz}}{\varepsilon_{xx}}$.

We aim to determine these Poisson ratios directly from the XRD data. Rather than computing the uniaxial strains as in the above definitions, we analyze the differential change of b and c with respect to a :

$$\nu_{xy} = -\left(\frac{a_0}{b_0}\right) \frac{db}{da}$$

$$\nu_{xz} = -\left(\frac{a_0}{c_0}\right) \frac{dc}{da}$$

As $a_0 = b_0$ in the tetragonal phase, the in-plane Poisson ratio reduces to $\nu_{xy} = -\frac{db}{da}$ and is thus independent of the zero-stress value.

In Figure S4 we plot b against a which clearly shows an enhanced value of the in-plane Poisson ratio near zero stress. The calculated slope $\frac{db}{da}$ is plotted against nominal strain in Figure S5(a). We perform a linear regression on ν_{xy} in a small nominal strain range of $\pm 0.75 \times 10^{-3}$ about the maximum value to extract the point value and fit value range, yielding the point/error bars in Figure S8(b). The Poisson ratio across the temperature range 74K-140K shows a clear diverging behavior.

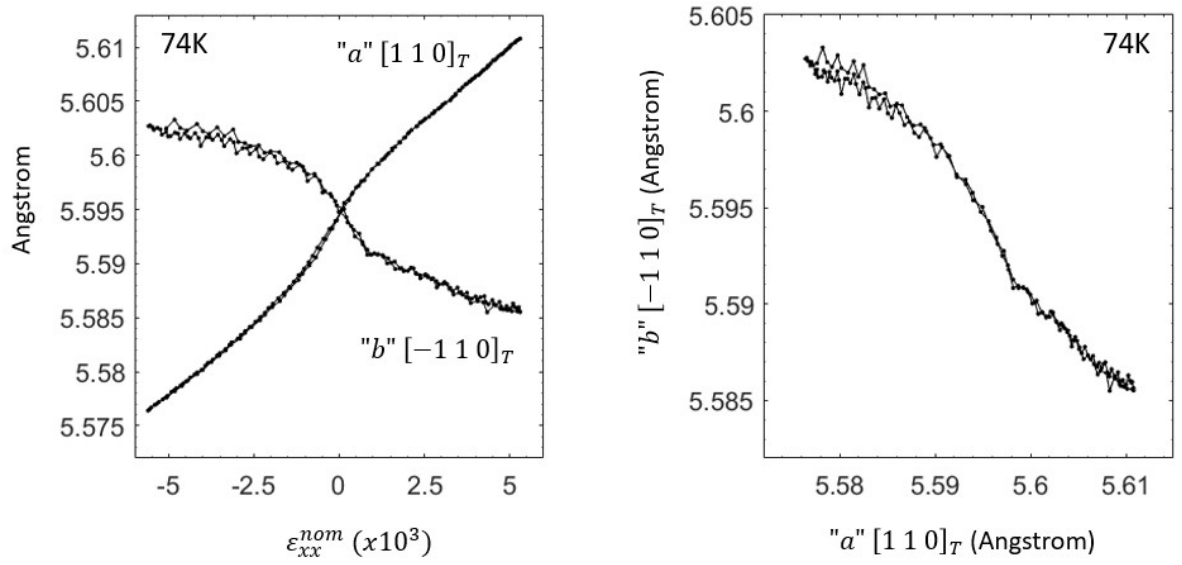


Figure S4. The in-plane a and b lattice constants vs nominal strain, and b vs a , at 74K.

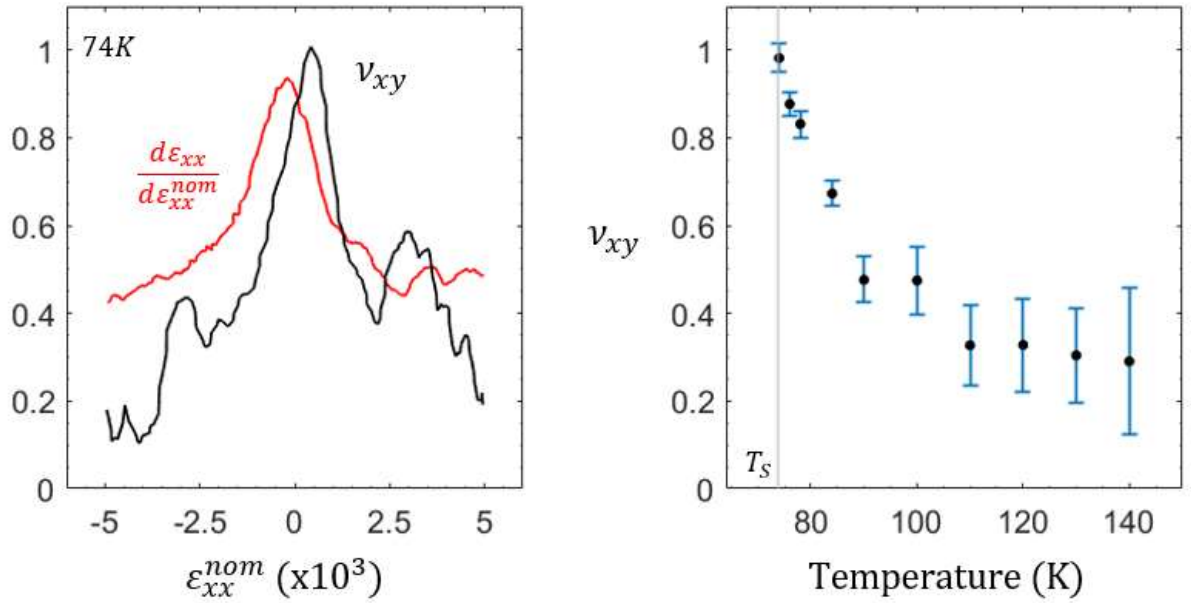


Figure S5. (a) The strain transmission $\frac{d\epsilon_{xx}}{d\epsilon_{xx}^{nom}}$ (red) and the in-plane Poisson ratio ν_{xy} (black) vs nominal strain at 74K (b) the Poisson ratio at peak value vs temperature shows a clear diverging behavior. Error bars are one standard deviation.

6. Extraction of Shear Modulus from Poisson Ratio.

In reference to the tetragonal unit cell basis, the uniaxial strains ε_{xx} , ε_{yy} , and ε_{zz} compose the antisymmetric B_{2g} and symmetric A_{1g} strains, defined as

$$\varepsilon_{B_{2g}} = \frac{1}{2}(\varepsilon_{xx} - \varepsilon_{yy}) = \frac{1}{2}\varepsilon_{xx}(1 + \nu_{xy})$$

$$\varepsilon_{A_{1g,1}} = \frac{1}{2}(\varepsilon_{xx} + \varepsilon_{yy}) = \frac{1}{2}\varepsilon_{xx}(1 - \nu_{xy})$$

$$\varepsilon_{A_{1g,2}} = \varepsilon_{zz} = -\varepsilon_{xx}\nu_{xz}$$

These are the irreducible representations into which all strains in a crystal with D_{4h} crystal symmetry can be decomposed for the uniaxial type of stress applied in our experiments. The strain $\varepsilon_{B_{2g}}$ is equivalent to the in-plane orthorhombicity that is created by the nematic order (ε in the main text), i.e. the nematicity and $\varepsilon_{B_{2g}}$ are both in the B_{2g} symmetry channel. The shear modulus C_{66} is also in this B_{2g} symmetry channel and so nematic fluctuations effectively soften the shear modulus. We may relate our applied uniaxial stress to the shear modulus through consideration of the full compliance tensor. However, given our choice for the xyz coordinate system, we must also rotate the compliance tensor from the tetragonal unit cell basis to our chosen xyz basis via a 45 degree rotation.

For a tetragonal crystal, the stiffness tensor takes the form

$$C = \begin{pmatrix} C_{11} & C_{12} & C_{13} & 0 & 0 & 0 \\ C_{12} & C_{11} & C_{13} & 0 & 0 & 0 \\ C_{13} & C_{13} & C_{33} & 0 & 0 & 0 \\ 0 & 0 & 0 & C_{44} & 0 & 0 \\ 0 & 0 & 0 & 0 & C_{44} & 0 \\ 0 & 0 & 0 & 0 & 0 & C_{66} \end{pmatrix}$$

The compliance tensor is the inverse of the stiffness tensor, so we have

$$S = C^{-1} = \begin{pmatrix} \frac{-C_{13}^2 + C_{11}C_{33}}{A} & \frac{-C_{13}^2 - C_{12}C_{33}}{A} & \frac{C_{13}}{B^+} & 0 & 0 & 0 \\ \frac{-C_{13}^2 - C_{12}C_{33}}{A} & \frac{-C_{13}^2 + C_{11}C_{33}}{A} & \frac{C_{13}}{B^+} & 0 & 0 & 0 \\ \frac{C_{13}}{B^+} & \frac{C_{13}}{B^+} & \frac{C_{13}}{B^-} & 0 & 0 & 0 \\ 0 & 0 & 0 & \frac{1}{C_{44}} & 0 & 0 \\ 0 & 0 & 0 & 0 & \frac{1}{C_{44}} & 0 \\ 0 & 0 & 0 & 0 & 0 & \frac{1}{C_{66}} \end{pmatrix}$$

where $A = \frac{-C_{13}^2 + C_{11}C_{33}}{(C_{11} - C_{12})(-2C_{13}^2 + C_{33}(C_{11} + C_{12}))}$ and $B^\pm = \pm(2C_{13}^2 - C_{33}(C_{11} + C_{12}))$.

This matrix is in the basis of the tetragonal lattice. We rotate the in-plane axes by 45 degrees with respect to this basis as

$$S' = K^{-T} S K^{-1}$$

where K is the rotation matrix given by

$$K = \begin{pmatrix} c^2 & c^2 & 0 & 0 & 0 & 2cs \\ c^2 & c^2 & 0 & 0 & 0 & -2cs \\ 0 & 0 & 1 & 0 & 0 & 0 \\ 0 & 0 & 0 & c & s & 0 \\ 0 & 0 & 0 & -s & c & 0 \\ -cs & cs & 0 & 0 & 0 & c^2 - s^2 \end{pmatrix}$$

and $c = \cos(45^\circ)$, $s = \sin(45^\circ)$.

This then gives the rotated compliance tensor:

$$S' = \begin{pmatrix} \frac{C_{33}}{-2B^-} + \frac{1}{4C_{66}} & \frac{C_{33}}{-2B^-} - \frac{1}{4C_{66}} & \frac{C_{13}}{B^+} & 0 & 0 & 0 \\ \frac{C_{33}}{-2B^-} - \frac{1}{4C_{66}} & \frac{C_{33}}{-2B^-} + \frac{1}{4C_{66}} & \frac{C_{13}}{B^+} & 0 & 0 & 0 \\ \frac{C_{13}}{B^+} & \frac{C_{13}}{B^+} & \frac{C_{11}+C_{12}}{B^-} & 0 & 0 & 0 \\ 0 & 0 & 0 & \frac{1}{2C_{44}} & 0 & 0 \\ 0 & 0 & 0 & 0 & \frac{1}{2C_{44}} & 0 \\ 0 & 0 & 0 & 0 & 0 & \frac{2}{C_{11}-C_{12}} \end{pmatrix}$$

Finally, the Poisson ratios are given by

$$\nu_{xy} = -\frac{\varepsilon_{yy}}{\varepsilon_{xx}} = -\frac{S'_{12}}{S'_{11}} = \frac{-C_{13}^2 + \frac{1}{2}(C_{11} + C_{12})C_{33} - C_{33}C_{66}}{-C_{13}^2 + \frac{1}{2}(C_{11} + C_{12})C_{33} + C_{33}C_{66}}$$

$$\nu_{xz} = -\frac{\varepsilon_{zz}}{\varepsilon_{xx}} = -\frac{S'_{13}}{S'_{11}} = \frac{2C_{13}C_{66}}{-C_{13}^2 + \frac{1}{2}(C_{11} + C_{12})C_{33} - C_{33}C_{66}}$$

We solve for the shear modulus C_{66} in terms of the in-plane Poisson ratio ν_{xy} as

$$C_{66} = \left(\frac{1}{2}(C_{11} + C_{12}) - \frac{C_{13}^2}{C_{33}} \right) \left(\frac{1 - \nu_{xy}}{1 + \nu_{xy}} \right)$$

We determine the magnitude from ultrasound data for an $x=0.037$ sample from ref. ²², using the measured values of C_{11} , C_{12} and C_{33} , and taking $C_{13} = \frac{1}{2}C_{12}$. The magnitude is nearly temperature-independent over this temperature range, reflecting the small impact that diverging nematic fluctuations have on the other elastic modulus terms. The exact value of the magnitude is not critical to our analysis as it only changes the fit parameter “ $C_{66,0}$ ” and not the temperature dependence. Still, the fitted value of $C_{66,0} = 38.8 \pm 4.7 \text{ GPa}$ is in excellent agreement with the high temperature limit of the measured C_{66} presented in ref ²². Using the values of ν_{xy} presented in Figure S5, we calculate C_{66} to yield Fig.4(e) in the main text.

In principle, we could also determine the shear modulus from the divergence of the out of plane Poisson ratio ν_{xz} . In this case, ν_{xz} approaches zero at T_S and so we encounter the difficulty of accurately

measuring a diminishing value. In contrast, ν_{xy} approaches its maximum value of 1 at T_S , giving stronger evidence that C_{66} actually does approach zero at the structural transition.

7. Free Energy Derivation.

We consider an Ising nematic order parameter ψ in a Landau free energy model:

$$F = \frac{a_0(T-T^*)}{2}\psi^2 + \frac{b}{4}\psi^4 + \frac{C_{66,0}}{2}\varepsilon^2 - \lambda\psi\varepsilon - h\varepsilon.$$

Here, T^* is the bare nematic transition temperature, $C_{66,0}$ is the bare elastic shear modulus, and ε is the orthorhombicity of the unit cell in the B_{2g} symmetry channel, i.e. in the symmetry channel of the nematic ordering. The nematic order parameter is linearly coupled to the orthorhombicity through the $\lambda\psi\varepsilon$ term. The lattice orthorhombicity is also linearly coupled to the externally applied stress h .

In the high-symmetry (tetragonal) phase, there is no static nematic order ($\langle\psi\rangle = 0$). Changing the strain state with a piezo actuator or other device induces nematicity via the nematic-elastic coupling. We define the $2m_{66}$ elastoresistivity coefficient in terms of the measured resistivity anisotropy $\eta = \frac{\rho_{xx}-\rho_{yy}}{\rho_{xx}+\rho_{yy}}$ and an applied strain ε as $2m_{66} = \frac{d\eta}{d\varepsilon}$. Minimizing the free energy first with respect to ψ and then to ε yields the nematic susceptibility, $\chi_N = \frac{\partial\psi}{\partial\varepsilon} = \frac{\lambda/a_0}{T-T^*}$. By symmetry, we take the resistivity anisotropy as linearly proportional to this induced nematicity, $\eta = k\psi$, and find that the $2m_{66}$ elastoresistivity coefficient is linearly proportional to the nematic susceptibility as $2m_{66} = k\chi_N$.

In the nematic (orthorhombic) phase under zero applied stress, a nematic order parameter ψ_0 develops which drives both a spontaneous structural orthorhombicity ε_0 and a spontaneous resistivity anisotropy η_0 . Minimizing the free energy with respect to ε yields the magnitude of the orthorhombicity, $\varepsilon_0 = \frac{\lambda}{C_{66,0}}\psi_0$. Assuming $\eta = k\psi$ remains valid in the ordered state, the ratio of the spontaneous resistivity anisotropy to the spontaneous orthorhombicity removes the dependencies on ψ of both and leaves only the temperature-independent ratio of the proportionality constants of both quantities as $\frac{\eta_0}{\varepsilon_0} = \left(\frac{k}{\frac{\lambda}{C_{66,0}}}\right)$.

We define the spontaneous elastoresistivity coefficient as $m_S = \frac{\eta_0}{\varepsilon_0}$.

Subbing $\varepsilon = \frac{\lambda}{C_{66,0}}\psi$ into the free energy and minimizing with respect to ψ , we obtain

$$\psi \left[a_0 \left(T - T^* - \frac{\lambda^2}{a_0 C_{66,0}} \right) + b\psi^2 \right] = 0$$

As the second term in the brackets is always positive, we find ψ may only have a nonzero value at $T < T^* + \frac{\lambda^2}{a_0 C_{66,0}}$, yielding an enhanced nematic transition temperature $T_S = T^* + \frac{\lambda^2}{a_0 C_{66,0}}$. The nematic order parameter grows with a mean-field temperature dependence as $\psi_0 = \sqrt{\frac{a_0}{b} (T_S - T)}$, and the spontaneous resistivity anisotropy and orthorhombicity are expected to follow the same temperature dependence within the nematic phase, i.e. $\varepsilon_0 \propto (T_S - T)^{\frac{1}{2}}$, $\eta_0 \propto (T_S - T)^{\frac{1}{2}}$.

We consider again the nematic susceptibility, $\chi_N = \frac{\lambda/a_0}{T - T^*}$, which diverges to the bare nematic transition temperature T^* and not to the enhanced T_S . However, at T_S the nematic susceptibility attains a finite value, $\chi_N(T_S) = \frac{\lambda/a_0}{T_S - T^*} = \frac{C_{66,0}}{\lambda}$. The corresponding value of $2m_{66}(T_S) = k\chi_N(T_S)$ is then $\frac{k}{\left(\frac{\lambda}{C_{66,0}}\right)}$, identical to the value of the **spontaneous elastoresistivity coefficient m_S** within the nematic phase. **Therefore, $2m_{66}$ is not only proportional to the nematic susceptibility, but can also directly measure the ratio of nematic coupling to the conduction electrons and to the lattice.**

Finally, we consider the effects of the diverging nematic susceptibility on the shear modulus. In the infinitesimal stress limit, we minimize the free energy with respect to ε and then to ψ and use $\frac{dh}{d\psi} = \frac{d\varepsilon}{d\psi} \frac{dh}{d\varepsilon} = \frac{C_{66}}{\chi_N}$ to obtain the renormalized shear modulus: $C_{66} = C_{66,0} - \lambda\chi_N$. As the nematic susceptibility approaches $\frac{C_{66,0}}{\lambda}$ at T_S , the shear modulus approaches zero.